

# Revealing the impact of chemical short-range order on radiation damage in MoNbTaVW high-entropy alloys using a machine-learning potential

Jiahui Liu,<sup>1,2</sup> Shuo Cao,<sup>1,2</sup> Yanzhou Wang,<sup>3</sup> Zheyong Fan,<sup>4, a)</sup> Guocai Lv,<sup>5</sup> Ping Qian,<sup>1</sup> and Yanjing Su<sup>1,2, b)</sup>

<sup>1)</sup>Beijing Advanced Innovation Center for Materials Genome Engineering, University of Science and Technology Beijing, Beijing 100083, China

<sup>2)</sup>Institute for Advanced Materials and Technology, University of Science and Technology Beijing, Beijing 100083, China

<sup>3)</sup>QTF Centre of Excellence, Department of Applied Physics, P.O. Box 15600, Aalto University, FI-00076 Aalto, Espoo, Finland

<sup>4)</sup>College of Physical Science and Technology, Bohai University, Jinzhou 121013, China

<sup>5)</sup>Basic Experimental Center of Natural Science, University of Science and Technology Beijing, Beijing 100083, China

(Dated: 17 July 2025)

The effect of chemical short-range order (CSRO) on primary radiation damage in MoNbTaVW high-entropy alloys is investigated using hybrid Monte Carlo/molecular dynamics simulations with a machine-learned potential. We show that CSRO enhances radiation tolerance by promoting interstitial diffusion while suppressing vacancy migration, thereby increasing defect recombination efficiency during recovery stage. However, CSRO is rapidly degraded under cumulative irradiation, with Warren-Cowley parameters dropping below 0.3 at a dose of only 0.03 dpa. This loss of ordering reduces the long-term enhancement of CSRO on radiation resistance. Our results highlight that while CSRO can effectively improve the radiation tolerance of MoNbTaVW, its stability under irradiation is critical to realizing and sustaining this benefit.

Tungsten (W)-based refractory high-entropy alloys (RHEAs) exhibit outstanding tolerance to high temperatures, stress, and irradiation, making them promising candidates for plasma-facing materials<sup>1–4</sup>. This class of high-entropy alloys (HEAs), composed of multiple principal elements at high concentrations, provides unprecedented flexibility in material design<sup>5,6</sup>. The resulting compositional complexity often promotes chemical short-range ordering (CSRO)<sup>7–10</sup>, which can profoundly influence their mechanical and functional properties<sup>11–15</sup>.

Given the experimental challenges in probing CSRO, molecular dynamics (MD) and Monte Carlo (MC) simulations have become essential tools for investigating its atomic-level impact on radiation damage. Liu *et al.* employed hybrid MC/MD simulations to examine the role of CSRO in radiation resistance<sup>16,17</sup>. Their results reveal that CSRO increases the migration energies of interstitials and vacancies, thereby suppressing defect migration and aggregation. Li *et al.* studied primary radiation damage in the Al<sub>0.5</sub>CoCrFeNi alloy and found that CSRO effectively suppresses point defect generation by increasing the formation energies of vacancies and interstitials, as well as the migration barriers of vacancies<sup>18</sup>. Additionally, Arkoub *et al.* used MD simulations to demonstrate that CSRO in Fe-Ni-Cr alloys evolves dynamically upon irradiation, either decreasing or increasing before reaching a steady-state value<sup>19</sup>. To date, most perspectives regarding the influence of CSRO on radiation damage have focused on face-centered cubic (fcc) multi-principal ele-

ment alloys (MPEAs). There is still a lack of large-scale atomistic simulations of radiation damage in RHEAs, with existing studies<sup>20–22</sup> primarily addressing the role of CSRO in segregation and threshold displacement energy (TDE). This is partly due to the need for larger systems and longer simulations in hybrid MC/MD studies of RHEAs, which substantially increases the computational cost.

Recently, a canonical-ensemble MC/MD algorithm has been implemented in the open-source GPUMD<sup>23</sup> package. In this approach<sup>24</sup>, the computational cost of each MC trial is independent of the system size and depends only on the average number of atomic neighbors. For sufficiently large systems (e.g., 490,000 atoms with an average coordination number  $M \approx 60$ ), the computational cost of MC steps becomes negligible, allowing the overall simulation speed to approach that of pure MD. This paves the way for large-scale simulations of the impact of CSRO on primary radiation damage.

In this study, all MC/MD simulations were performed using GPUMD with a neuroevolution potential (NEP) model<sup>25,26</sup> constructed for Mo-Nb-Ta-V-W systems<sup>27</sup> based on the training dataset of a tabulated Gaussian approximation potential (tabGAP) model<sup>21,28,29</sup>. The NEP approach is a highly computationally efficient approach that has found widespread applications in compositionally complex materials<sup>30</sup>. To validate its accuracy, we first reproduced CSRO-related simulations previously conducted with the tabGAP model, including (i) ordering and segregation in a single-crystal equiatomic RHEA, and (ii) threshold displacement energy calculations. As shown in Supplementary Fig. 1, Mo and Ta exhibit local ordering at low temperatures. Mo-Nb and W-V first-nearest-neighbor (1NN) pairs are also favored,

<sup>a)</sup>Electronic mail: [brucenju@gmail.com](mailto:brucenju@gmail.com)

<sup>b)</sup>Electronic mail: [yjsu@ustb.edu.cn](mailto:yjsu@ustb.edu.cn)



with W-V additionally showing second-nearest neighbor (2NN) attraction, suggesting more complex local structures. Above 300 K, the ordered phases gradually transition into a random solid solution (RSS). Supplementary Fig. 2 shows the angular maps of TDEs for the five primary knock-on atom (PKA) types in the SRO-HEA, with values of 60 eV (V), 62 eV (Nb), 55 eV (Mo), 52 eV (Ta), and 50 eV (W), averaging 56 eV. Supplementary Fig. 3 compares the distributions between the SRO-HEA and the reference RSS-HEA<sup>27</sup>. CSRO leads to an upward shift of about 5 eV in both the distribution and average. All results above are consistent with previous findings based on the tabGAP model<sup>21,22</sup>. Additional computational details are provided in the Supplementary Notes.

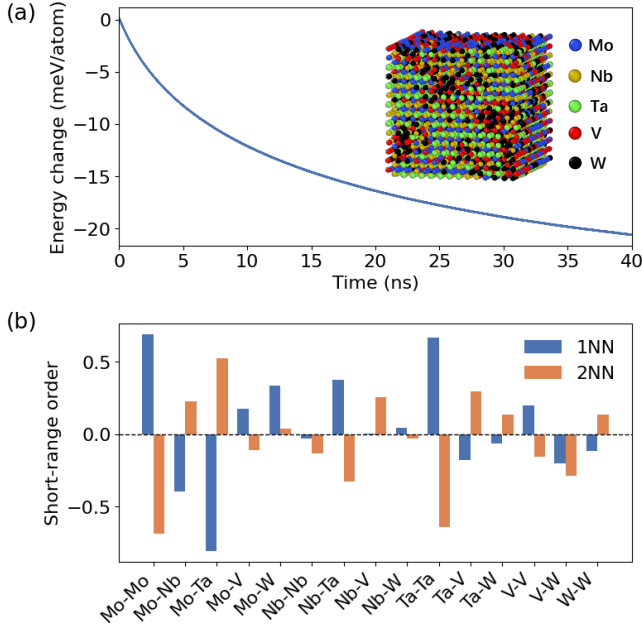


FIG. 1. (a) Potential energy change from the random alloy to an ordered structure as a function of MD simulation time. (b) First-nearest-neighbor and second-nearest-neighbor Warren-Cowley parameters in the short-range ordered alloy. The inset in (a) shows a representative local atomic configuration exhibiting short-range order.

After evaluating the reliability of the NEP model in describing CSRO and atomic displacements, we prepared a large SRO-HEA system with simulation box dimensions of  $150a_0 \times 150a_0 \times 150a_0$  (6,750,000 atoms) to investigate the impact of CSRO on radiation damage in MoNbTaVW HEAs. Figure 1(a) shows the potential energy as a function of time during hybrid MC/MD equilibration under the isothermal-isobaric ensemble at 300 K, with 100 MC trails every 10 MD steps. Figure 1(b) presents the 1NN and 2NN Warren-Cowley (WC) parameters in the final configuration. The WC parameter<sup>31</sup> for an element pair AB is computed as

$$\alpha_{AB} = 1 - \frac{p^{AB}}{c_B}, \quad (1)$$

where  $p^{AB}$  is the probability of finding a B atom at a nearest-neighbor site of an A atom, and  $c_B$  is the concentration of element B in the alloy. A negative  $\alpha_{AB}$  suggests a tendency toward ordering between A and B atoms, while a positive value means repulsion. Although the larger system size here leads to a slight reduction in WC parameters compared to smaller system size, the chemical ordering is maintained, confirming that the 40 ns simulation is sufficient to establish well-developed CSRO. The inset in Fig. 1(a) shows a local atomic snapshot, in which Mo-Ta pairs exhibit an almost perfect B2-type ordering.

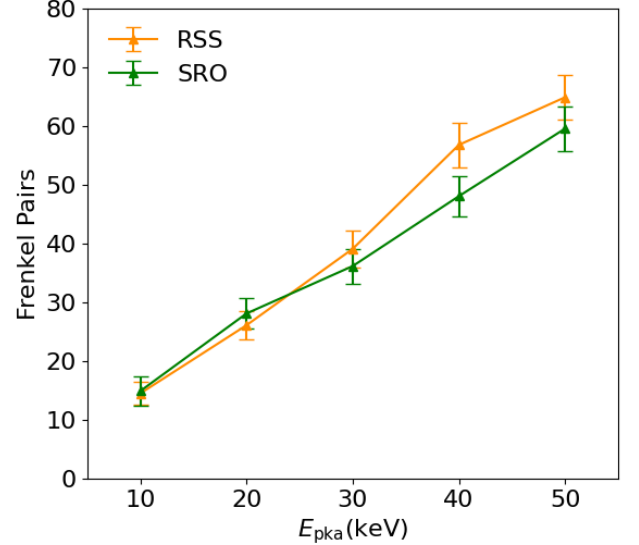


FIG. 2. The residual point defects in random and short-range ordered alloys. Error bars represent the standard deviations from 40 independent simulations.

Displacement cascade simulations were then performed on both CSRO and RSS MoNbTaVW HEAs at PKA energies of 10, 20, 30, 40, and 50 keV. To ensure statistical convergence and stable results, 40 simulations were carried out for each PKA energy, each lasting about 50 ps. For the SRO-HEAs, the prepared configuration was randomly shifted before each recoil event to sample different local chemical environments. For the RSS-HEAs, a same-sized random equimolar body-centered cubic (bcc) cell was generated and equilibrated at 300 K and 0 GPa for 30 ps prior to each simulation. The central atom was selected as the PKA and given an initial velocity in a random direction. A Nosé-Hoover chain thermostat<sup>32</sup> was applied to a 10 Å-thick boundary region, while all other atoms evolved under the NVE ensemble. The time step was dynamically adjusted to limit the maximum atomic displacement to 0.015 Å per step, with an upper bound of 1 fs. Electronic stopping<sup>33</sup> was applied as a frictional force on atoms with a kinetic energy over 10 eV, using data from the SRIM-2013 code<sup>34,35</sup>. All reported results are statistical averages over the 40 independent simulations.



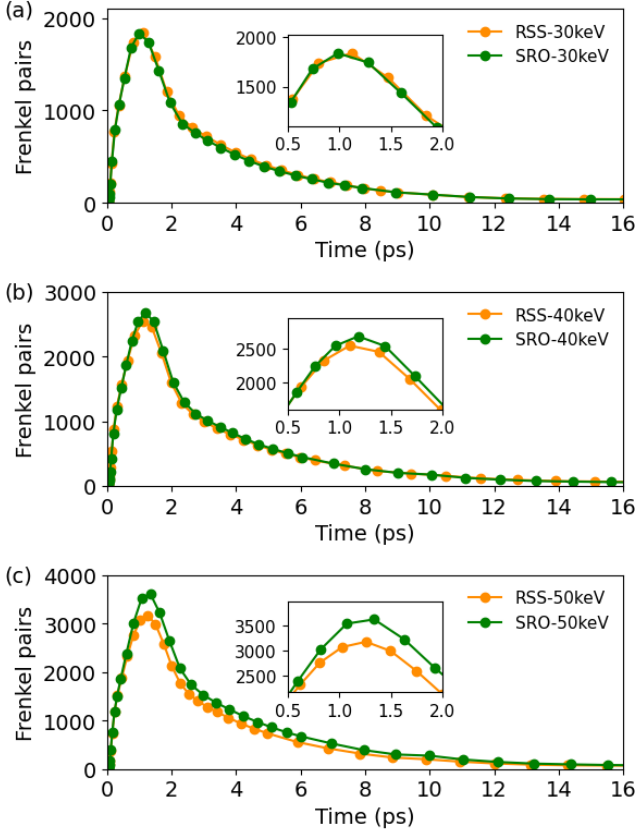


FIG. 3. The number of Frenkel pairs as a function of simulation time in random and short-range ordered alloys during cascade simulations at (a) 30 keV, (b) 40 keV, and (c) 50 keV.

Figure 2 shows the average number of Frenkel pairs (FPs) that survived at the final stage of the cascade simulations in both the SRO-HEAs and RSS-HEAs. Although CSRO increases the TDE, the number of FPs at lower energies (10 and 20 keV) remains comparable between the two systems. As the PKA energy increases, SRO-HEAs exhibit a notable suppression in the number of surviving point defects. Figure 3 presents the time evolution of the number of FPs during the cascade process at PKA values of 30, 40, and 50 keV. At higher energies, more FPs are generated in SRO-HEAs during the thermal spike stage, possibly due to less efficient energy dissipation in chemically ordered regions, which leads to a larger molten zone in the cascade core. The energy loss to electronic interactions, listed in the Supplementary Table 1, is nearly identical between the SRO-HEA and RSS-HEA systems across all PKA energies. Taken together, the increased defect recombination and comparable electronic energy loss indicate that the thermal relaxation phase plays a significant role. Moreover, Supplementary Fig. 4 shows the WC parameters in the molten region after cooling. The persistence of CSRO likely affects the migration of interstitial atoms and the recombination of FPs during the recovery stage.

To further investigate defect evolution during the re-

covery stage, we simulated the diffusion of a single interstitial and a single vacancy in both SRO-HEAs and RSS-HEAs. Equiatomic random solid solutions of  $16a_0 \times 16a_0 \times 16a_0$  unit cells (8192 atoms) were constructed, with the SRO system equilibrated using hybrid MC/MD at 300 K for 1 ns. An interstitial was introduced by adding one extra W atom to the perfect cell (8193 atoms), and a vacancy was created by removing one random atom (8191 atoms). Prior to diffusion simulations, the SRO and RSS systems were equilibrated at temperatures ranging from 2200 K to 2600 K (in 100 K intervals) and zero pressure for 10 ps in the NPT ensemble. Diffusion was simulated for 10 ns in the NVE ensemble with a correlation time of 1 ns, and both average and elemental mean squared displacements (MSDs) were computed. The temporal evolution of elemental and average MSDs for interstitial and vacancy diffusion is presented in Supplementary Fig. 5 and 6. For interstitial diffusion, V atoms dominate the overall migration, especially in the SRO-HEAs, where the diffusion of Nb, Ta, and Mo atoms becomes markedly non-linear. It is worth noting that V atoms are the primary interstitial defects generated during the radiation damage of MoNbTaVW. In the case of vacancy diffusion, all MSDs increase approximately linearly with time. However, in SRO-HEAs, vacancy migration is noticeably suppressed.

Subsequently, the tracer diffusion coefficients  $D^*$  were calculated from the slope of the MSD as a function of time, according to the Einstein relation<sup>36</sup>:

$$D^* = \frac{\text{MSD}(t)}{6t}. \quad (2)$$

Figure 4(a) and (b) show the average and elemental tracer diffusion coefficients for interstitials in the RSS-HEAs and SRO-HEAs. In the RSS-HEAs, the elemental tracer diffusion coefficients follow the order  $V > \text{Mo} > \text{W} \approx \text{Nb} > \text{Ta}$ , and only the interstitial tracer diffusion coefficient ( $D_{\text{Int}}^*$ ) of V exceeds the average value across the temperature range. Notably, in the SRO-HEAs, the diffusion of Mo, Nb, and Ta is significantly suppressed, likely due to the formation of Mo-Ta and Mo-Nb CSRO. Figure 4(c) and (d) show the average and elemental tracer diffusion coefficients for vacancy diffusion in the RSS-HEAs and SRO-HEAs. The vacancy tracer diffusion coefficient ( $D_{\text{Vac}}^*$ ) values of V and Nb are higher than the average ones in both systems. In contrast, the tracer diffusion coefficients of Mo and Ta in the SRO-HEAs exhibit considerable fluctuations, as CSRO affects vacancy diffusion.

The migration energy  $E_m$  was obtained by fitting the Arrhenius equation<sup>37,38</sup>:

$$D^* = D_0 e^{-\frac{E_m}{k_B T}}, \quad (3)$$

where  $D_0$  is the pre-exponential factor,  $k_B$  is the Boltzmann constant and  $T$  is the temperature. The migration energies of interstitials and vacancies in the RSS-HEA are  $E_m^{\text{int}} = 1.33 \pm 0.08$  eV and  $E_m^{\text{vac}} = 1.10 \pm 0.11$  eV, which



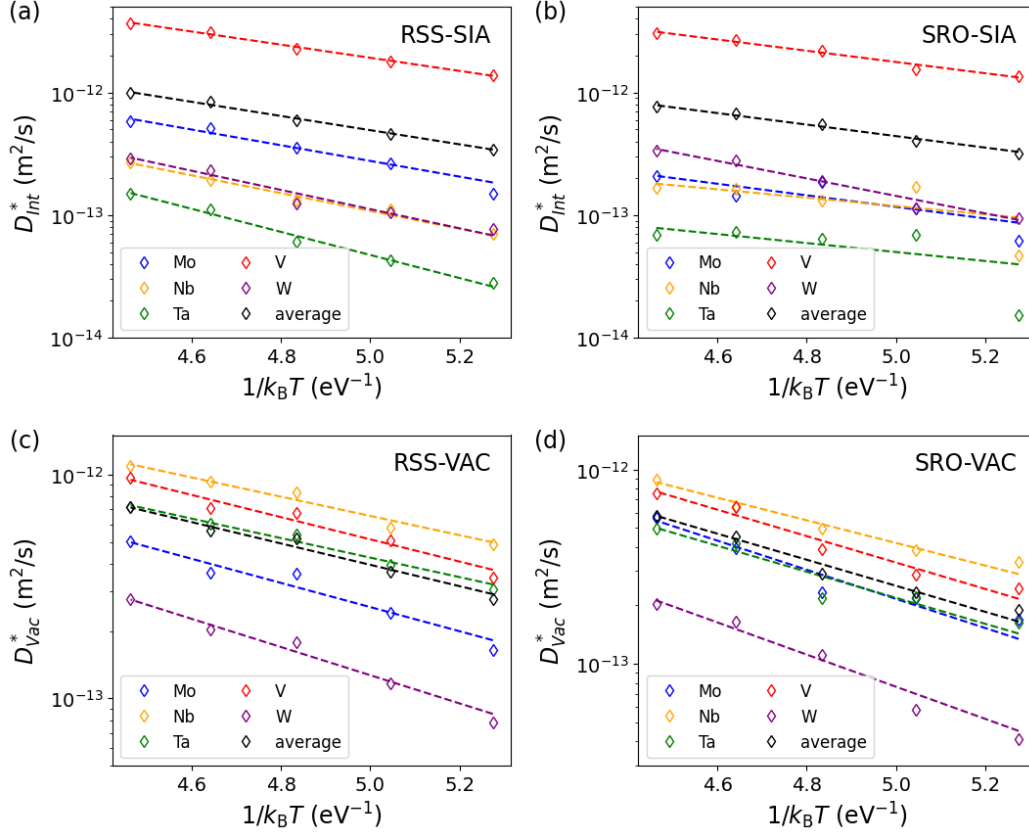


FIG. 4. Tracer diffusion coefficients of elements for interstitial diffusion in (a) random and (b) short-range ordered alloys, and for vacancy diffusion in (c) random and (d) short-range ordered alloys.

are consistent with the values reported using the tabGAP model<sup>39</sup>. In contrast, the migration energies in the SRO-HEA are  $E_m^{\text{int}} = 1.08 \pm 0.08$  eV and  $E_m^{\text{vac}} = 1.54 \pm 0.14$  eV. The presence of CSRO, particularly the formation of Mo-Ta and Mo-Nb pairs, effectively influences defect diffusion by enhancing interstitial migration while suppressing vacancy migration. This imbalance leads to more frequent recombination of point defects during the recovery stage, thereby improving the material's resistance to irradiation damage.

Although the CSRO is maintained during the primary radiation damage, the inherent tendency of MoNbTaVW to transform toward a RSS configuration at elevated temperatures may lead to its degradation as the radiation dose accumulates. To evaluate the stability of the CSRO, a series of overlapping cascades were simulated as cumulative single-cascade events, each followed by a brief relaxation run. The dose after  $N$  cascades, in units of displacements per atom (dpa), was calculated according to the Norgett-Robinson-Torrens displacements per atom (NRT-dpa) model<sup>40</sup>, using a damage energy of  $T_d = 10$  keV. The simulation box, with dimensions of  $100a_0 \times 100a_0 \times 100a_0$  (2,000,000 atoms), was sufficiently large to prevent cascades from interacting with the simulation boundaries in SRO-HEAs. A total of 1000 cascades were simulated sequentially, resulting in an accumulated

dose of approximately 0.03 dpa, which corresponds to a relatively low irradiation dose. Figure 5 shows the WC parameters as a function of dose for both (a) 1NN and (b) 2NN pairs. As shown, the CSRO is rapidly degraded with increasing dose. At a dose of 0.03 dpa, the absolute values of the WC parameters drop below 0.3, indicating a weak level of chemical ordering. This highlights that although CSRO enhances radiation resistance, maintaining its stability under increasing radiation dose is essential to sustaining this improvement.

In summary, our hybrid MC/MD simulations with the neuroevolution potential provide novel insights into how CSRO influences radiation damage behavior in MoNbTaVW HEAs. The presence of CSRO enhances radiation resistance by facilitating interstitial diffusion and suppressing vacancy migration at higher PKA energies, thereby increasing the defect recombination efficiency. However, the CSRO is rapidly degraded with increasing radiation dose. Thus, utilizing CSRO to enhance the radiation tolerance of MoNbTaVW is a viable strategy, provided that its stability can be improved. This may be achieved, for instance, through the introduction of grain boundaries or phase interfaces.

#### Data availability

The data presented in this paper are available from the corresponding authors upon reasonable request.



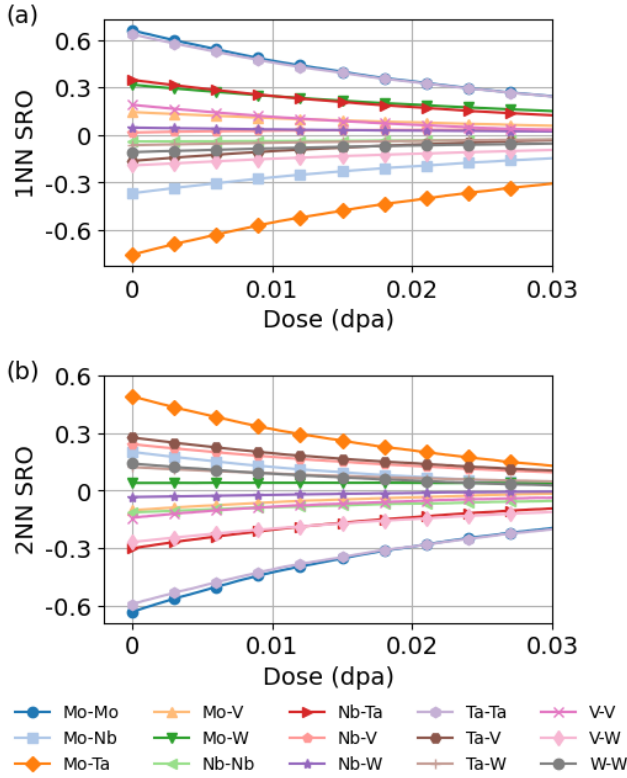


FIG. 5. Evolution of (a) first-nearest-neighbor and (b) second-nearest-neighbor Warren-Cowley parameters with dose in the short-range ordered alloy.

**Acknowledgments** This work was supported by the National Science and Technology Advanced Materials Major Program of China (No. 2024ZD0606900), and USTB MatCom of Beijing Advanced Innovation Center for Materials Genome Engineering.

- <sup>1</sup>O. Senkov, G. Wilks, D. Miracle, C. Chuang, and P. Liaw, “Refractory high-entropy alloys,” *Intermetallics* **18**, 1758–1765 (2010).
- <sup>2</sup>O. Senkov, G. Wilks, J. Scott, and D. Miracle, “Mechanical properties of nb25mo25ta25w25 and v20nb20mo20ta20w20 refractory high entropy alloys,” *Intermetallics* **19**, 698–706 (2011).
- <sup>3</sup>O. El-Atwani, N. Li, M. Li, A. Devaraj, J. K. S. Baldwin, M. M. Schneider, D. Sobieraj, J. S. Wróbel, D. Nguyen-Manh, S. A. Maloy, and E. Martinez, “Outstanding radiation resistance of tungsten-based high-entropy alloys,” *Science Advances* **5**, eaav2002 (2019).
- <sup>4</sup>O. El Atwani, H. T. Vo, M. A. Tunes, C. Lee, A. Alvarado, N. Krienke, J. D. Poplawsky, A. A. Kohnert, J. Gigax, W.-Y. Chen, M. Li, Y. Q. Wang, J. S. Wróbel, D. Nguyen-Manh, J. K. S. Baldwin, O. U. Tukac, E. Aydogan, S. Fensin, and E. Martinez, “A quinary wtacrvhf nanocrystalline refractory high-entropy alloy withholding extreme irradiation environments,” *Nature Communications* **14**, 2516 (2023).
- <sup>5</sup>J.-W. Yeh, S.-K. Chen, S.-J. Lin, J.-Y. Gan, T.-S. Chin, T.-T. Shun, C.-H. Tsau, and S.-Y. Chang, “Nanostructured high-entropy alloys with multiple principal elements: Novel alloy design concepts and outcomes,” *Advanced Engineering Materials* **6**, 299–303 (2004).
- <sup>6</sup>D. Miracle and O. Senkov, “A critical review of high entropy alloys and related concepts,” *Acta Materialia* **122**, 448–511 (2017).

- <sup>7</sup>B. Jiang, C. A. Bridges, R. R. Unocic, K. C. Pitike, V. R. Cooper, Y. Zhang, D.-Y. Lin, and K. Page, “Probing the local site disorder and distortion in pyrochlore high-entropy oxides,” *Journal of the American Chemical Society* **143**, 4193–4204 (2021).
- <sup>8</sup>F. Walsh, A. Abu-Odeh, and M. Asta, “Reconsidering short-range order in complex concentrated alloys,” *MRS Bulletin* **48**, 753–761 (2023).
- <sup>9</sup>M. Xu, S. Wei, C. C. Tasan, and J. M. LeBeau, “Determination of short-range order in tivnbhf(al),” *Applied Physics Letters* **122**, 181901 (2023).
- <sup>10</sup>K. Sheriff, Y. Cao, T. Smidt, and R. Freitas, “Quantifying chemical short-range order in metallic alloys,” *Proceedings of the National Academy of Sciences* **121**, e2322962121 (2024).
- <sup>11</sup>E. P. George, D. Raabe, and R. O. Ritchie, “High-entropy alloys,” *Nature Reviews Materials* **4**, 515–534 (2019).
- <sup>12</sup>P. A. Santos-Florez, S.-C. Dai, Y. Yao, H. Yanxon, L. Li, Y.-J. Wang, Q. Zhu, and X.-X. Yu, “Short-range order and its impacts on the bcc monbtaw multi-principal element alloy by the machine-learning potential,” *Acta Materialia* **255**, 119041 (2023).
- <sup>13</sup>W.-R. Jian, S. Xu, D. Chen, and I. J. Beyerlein, “Chemical short-range order enhances fracture toughness of medium entropy alloy cocrni,” *Applied Physics Letters* **124**, 171903 (2024).
- <sup>14</sup>S. Ma, W. Liu, Q. Li, J. Zhang, S. Huang, Y. Xiong, B. Xu, T. Yang, and S. Zhao, “Mechanism of elemental segregation around extended defects in high-entropy alloys and its effect on mechanical properties,” *Acta Materialia* **264**, 119537 (2024).
- <sup>15</sup>X. Zhao, H. Huang, Y. Su, L. Qiao, and Y. Yan, “Exploring high corrosion-resistant refractory high-entropy alloy via a combined experimental and simulation study,” *npj Materials Degradation* **8**, 77 (2024).
- <sup>16</sup>L. Liu, X. Liu, Q. Du, H. Wang, Y. Wu, S. Jiang, and Z. Lu, “Local chemical ordering and its impact on radiation damage behavior of multi-principal element alloys,” *Journal of Materials Science & Technology* **135**, 13–25 (2023).
- <sup>17</sup>L. Liu, W. Li, H. Wang, Y. Wu, S. Jiang, X. Zhang, X. Liu, and Z. Lu, “Impacts of local chemical ordering on the primary radiation damage in Cr-Fe-Ni multi-principal element alloys,” *Progress in Natural Science: Materials International* **34**, 178–186 (2024).
- <sup>18</sup>G. Li, L. Yuan, J. Li, M. Zhang, and D. Li, “Effect of Al related chemical short-range order on the irradiation resistance of Al0.5CoCrFeNi multi-principal element alloy: A molecular dynamics simulation,” *Materials Today Communications* **38**, 108302 (2024).
- <sup>19</sup>H. Arkoub and M. Jin, “Impact of chemical short-range order on radiation damage in fe-ni-cr alloys,” *Scripta Materialia* **229**, 115373 (2023).
- <sup>20</sup>X.-G. Li, C. Chen, H. Zheng, Y. Zuo, and S. P. Ong, “Complex strengthening mechanisms in the nbmotaw multi-principal element alloy,” *npj Computational Materials* **6**, 70 (2020).
- <sup>21</sup>J. Byggmästar, K. Nordlund, and F. Djurabekova, “Modeling refractory high-entropy alloys with efficient machine-learned interatomic potentials: Defects and segregation,” *Physical Review B* **104**, 104101 (2021).
- <sup>22</sup>J. Byggmästar, F. Djurabekova, and K. Nordlund, “Threshold displacement energies in refractory high-entropy alloys,” *Physical Review Materials* **8**, 115406 (2024).
- <sup>23</sup>Z. Fan, W. Chen, V. Vierimaa, and A. Harju, “Efficient molecular dynamics simulations with many-body potentials on graphics processing units,” *Computer Physics Communications* **218**, 10–16 (2017).
- <sup>24</sup>K. Song, J. Liu, S. Chen, Z. Fan, Y. Su, and P. Qian, “Solute segregation in polycrystalline aluminum from hybrid monte carlo and molecular dynamics simulations with a unified neuroevolution potential,” (2024), arXiv:2404.13694 [cond-mat.mtrl-sci].
- <sup>25</sup>Z. Fan, Z. Zeng, C. Zhang, Y. Wang, K. Song, H. Dong, Y. Chen, and T. Ala-Nissila, “Neuroevolution machine learning potentials: Combining high accuracy and low cost in atomistic simulations and application to heat transport,” *Physical Review B* **104**,



- 104309 (2021).
- <sup>26</sup>K. Song, R. Zhao, J. Liu, Y. Wang, E. Lindgren, Y. Wang, S. Chen, K. Xu, T. Liang, P. Ying, N. Xu, Z. Zhao, J. Shi, J. Wang, S. Lyu, Z. Zeng, S. Liang, H. Dong, L. Sun, Y. Chen, Z. Zhang, W. Guo, P. Qian, J. Sun, P. Erhart, T. Ala-Nissila, Y. Su, and Z. Fan, “General-purpose machine-learned potential for 16 elemental metals and their alloys,” *Nature Communications* **15**, 10208 (2024).
  - <sup>27</sup>J. Liu, J. Byggmästar, Z. Fan, B. Bai, P. Qian, and Y. Su, “Utilizing a machine-learned potential to explore enhanced radiation tolerance in the monbtavw high-entropy alloy,” (2024), arXiv:2411.02834 [cond-mat.mtrl-sci].
  - <sup>28</sup>J. Byggmästar, K. Nordlund, and F. Djurabekova, “Gaussian approximation potentials for body-centered-cubic transition metals,” *Physical Review Materials* **4**, 093802 (2020).
  - <sup>29</sup>J. Byggmästar, K. Nordlund, and F. Djurabekova, “Simple machine-learned interatomic potentials for complex alloys,” *Physical Review Materials* **6**, 083801 (2022).
  - <sup>30</sup>P. Ying, C. Qian, R. Zhao, Y. Wang, K. Xu, F. Ding, S. Chen, and Z. Fan, “Advances in modeling complex materials: The rise of neuroevolution potentials,” *Chemical Physics Reviews* **6**, 011310 (2025).
  - <sup>31</sup>J. M. Cowley, “An approximate theory of order in alloys,” *Phys. Rev.* **77**, 669–675 (1950).
  - <sup>32</sup>G. J. Martyna, M. L. Klein, and M. Tuckerman, “Nosé–hoover chains: The canonical ensemble via continuous dynamics,” *The Journal of Chemical Physics* **97**, 2635–2643 (1992).
  - <sup>33</sup>K. Nordlund, “Molecular dynamics simulation of ion ranges in the 1–100 keV energy range,” *Computational Materials Science* **3**, 448–456 (1995).
  - <sup>34</sup>J. F. Ziegler, M. Ziegler, and J. Biersack, “Srim – the stopping and range of ions in matter (2010),” *Nuclear Instruments and Methods in Physics Research Section B: Beam Interactions with Materials and Atoms* **268**, 1818–1823 (2010).
  - <sup>35</sup>J. Ziegler, “Srim-2013 software package,” (2013), available online at <http://www.srim.org>.
  - <sup>36</sup>A. Einstein, “Über die von der molekularkinetischen theorie der wärme geforderte bewegung von in ruhenden flüssigkeiten suspendierten teilchen,” *Annalen der Physik* **322**, 549–560 (1905).
  - <sup>37</sup>J. Zhang, C. Gadelmeier, S. Sen, R. Wang, X. Zhang, Y. Zhong, U. Glatzel, B. Grabowski, G. Wilde, and S. V. Divinski, “Zr diffusion in bcc refractory high entropy alloys: A case of ‘non-sluggish’ diffusion behavior,” *Acta Materialia* **233**, 117970 (2022).
  - <sup>38</sup>V. Kulitckii, A. Schneider, O. Lukianova, G. Wilde, C.-C. Fu, and S. Divinski, “Atomic diffusion in bcc fe–mn alloys: Theoretical analysis and experimental measurements across the curie temperature,” *Acta Materialia* **251**, 118883 (2023).
  - <sup>39</sup>G. Wei, J. Byggmästar, J. Cui, K. Nordlund, J. Ren, and F. Djurabekova, “Revealing the critical role of vanadium in radiation damage of tungsten-based alloys,” *Acta Materialia* **274**, 119991 (2024).
  - <sup>40</sup>M. J. Norgett, M. T. Robinson, and I. M. Torrens, “A proposed method of calculating displacement dose rates,” *Nuclear Engineering and Design* **33**, 50–54 (1975).